Volume 22
Number 13
1 April 2026
Pages 2459–2588

Soft Matter

rsc.li/soft-matter-journal

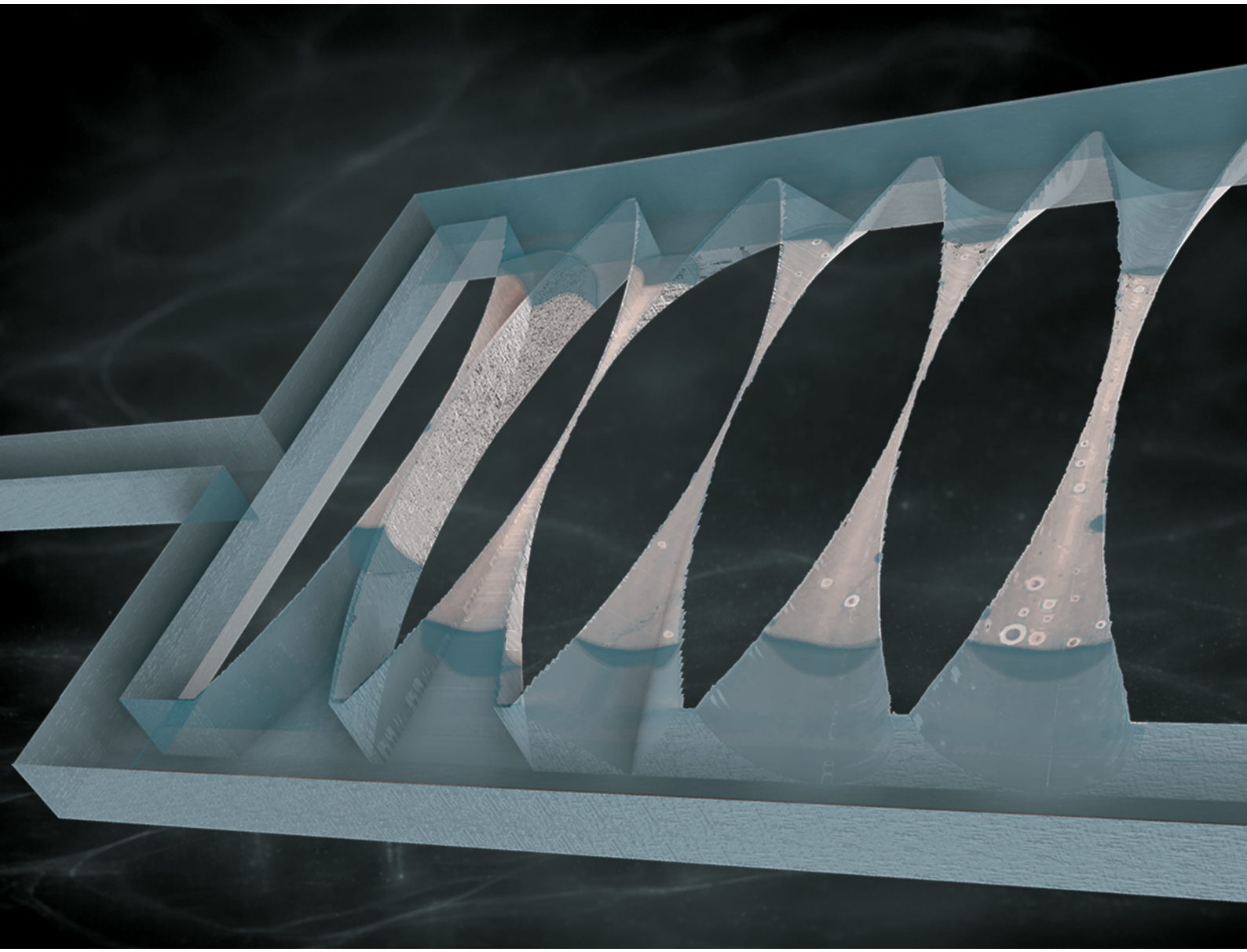

ISSN 1744-6848

ROYAL SOCIETY OF CHEMISTRY

COMMUNICATION
Kelsey Yao and Shaina Kelly
Replicable 2.5D PDMS microfluidics with precision nanoscale features expand the dimensions of pore-scale flow studies

Soft Matter

COMMUNICATION

View Article Online
View Journal | View Issue

Cite this: *Soft Matter*, 2026, **22**, 2466

Received 1st October 2025,
Accepted 10th February 2026

DOI: 10.1039/d5sm01004g

rsc.li/soft-matter-journal

Replicable 2.5D PDMS microfluidics with precision nanoscale features expand the dimensions of pore-scale flow studies

Kelsey Yao and Shaina Kelly *

Customizable 2.5D microfluidic chips, tailored for rock-on-a-chip studies, are developed using direct laser writing (DLW) and soft lithography. Chip microchannels feature varied cross-sectional shape and height, convergences as small as 1–2 μm, and controlled nanoscale surface roughness. The impact of these 2.5D features on pore-scale transport phenomena is demonstrated with trapped bubble dissolution experiments.

Introduction

Microfluidic and nanofluidic devices are established tools for studying fundamental pore-scale flow phenomena, including pore-scale advection and diffusion,[1,2] capillarity,[3] phase transition,[4] mixing,[5] and crystallization dynamics.[6] Lab-on-a-chip platforms enable advanced study of these phenomena for a myriad of energy, environmental, and biologic porous media applications including sustainable hydrocarbon[7] and critical minerals recovery,[8] carbon storage,[9,10] geothermal energy,[11] environmental remediation,[12] water treatment,[13] tissue engineering,[14] drug delivery,[15] and cement enhancements.[16] Many investigators have generated "reservoir/rock-on-a-chip"[17–22] and "organ-on-a-chip"[23,24] platforms to mimic the pore structures of, respectively, *in situ* rocks and soils and *in vivo* tissues.

Common fabrication processes for both micro- and nanofluidics include photolithography and etching[20,21] – top-down fabrication methods that allow precise patterning of nanostructures onto substrates like silicon or glass (see an extended summary of current fabrication processes in SI, Section 1). However, these techniques only replicate pore-scale geometries in the x–y plane, resulting in geometries of uniform depth (*i.e.*, 2D microfluidics). Further, these planar designs are intrinsically limited in cross-sectional shape (typically rectangles or trapezoids).[25,26] 2D geometric limitations can bias capillarity and flow patterns, among other phenomena, reducing the scalability of microfluidic results to real-world porous media and limiting the study of confinement effects.[3,18,19,27] Rock-on-a-chip platforms in particular typically fall short in replicating the complex pore structures (see SI Fig. S1 examples), dual-porosity aspect ratios (nanoporous regions connecting micro/macropores), and tortuosity generated in geologic porous media by varied depositional and diagenetic processes.[28,29] Hence, one of the next frontiers for lab-on-a-chip technology, particularly rock-on-a-chip studies, is extending microfluidic fabrication capabilities to consistently and cost-effectively enable control over axial variations in channel cross-sectional shape, height, and inlaid features within the same chip – *i.e.*, replicable 2.5D microfluidics.

2.5D microfluidics can be produced by modifying traditional etching fabrication techniques[19,30] or direct laser writing (DLW). In particular, grayscale lithography (GSL), a variant of conventional photolithography, varies the intensity of light exposure to obtain a continuous range of resist heights after development.[31] This technique has been used to make 2.5D channels with submicron depths and lateral widths as small as 2 μm, but lateral resolution and control over cross-sectional shape are both limited by beam size.[32] In DLW, lasers precisely crosslink a photosensitive resin to 3D-print structures with a resolution on the order of 100 nm.[26,33,34] DLW stands out in achieving high-resolution and complex 2.5–3D geometries, but is limited by low throughput and high equipment costs. Because modifications to traditional lithography, including GSL, hinge upon layer-by-layer fabrication from the x–y plane, they generally fall short in achieving the precision cross-sectional shapes and smooth depth variations attained with DLW.

In this communication, we use DLW to create reusable molds featuring 2.5D customizable cross-sectional profiles and channel depths emulating critical constrictions (*e.g.*, pore throats, microfractures, grain boundaries) commonly found in geologic porous media (see Fig. 1a and SI Fig. S1). Soft lithography is then used to replicate the geometry into polydimethylsiloxane (PDMS) polymer chips, with the option of

Department of Earth and Environmental Engineering, Columbia University, New York, USA. E-mail: sak2280@columbia.edu

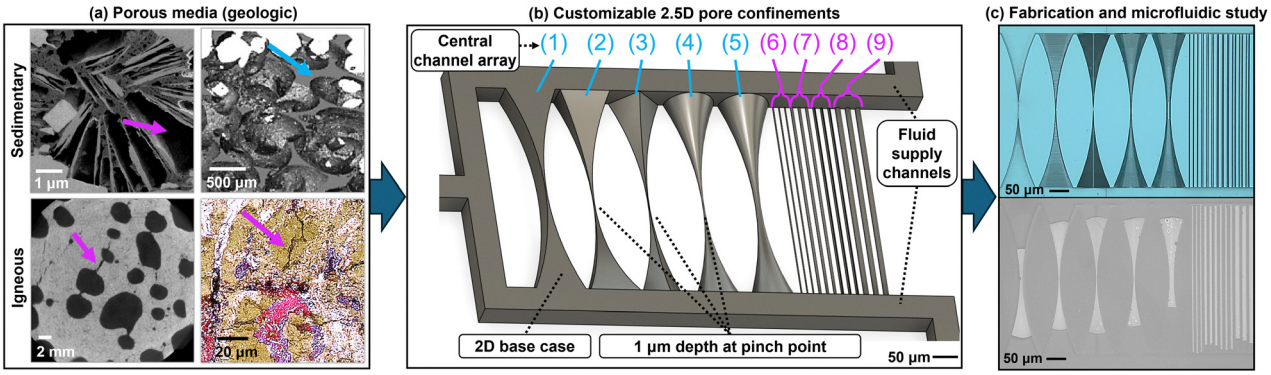

Fig. 1 (a) Examples of geologic porous materials. Clockwise from top left: focused ion beam-scanning electron microscopy (FIB-SEM) image of shale;[39] 3D pore-space image of oolitic limestone from three-dimensional micro-CT images;[40] thin section of Newberry basalt; micro-CT image of American Samoa basalt. (b) Schematic of central channel array and U-shaped fluid supply channel, as designed for the DLW mold (positive geometry). Blue arrows and purple arrows in (a) highlight pore throats similar to channels #1–#5 and to channels #6–#9, respectively, of the featured microfluidic design shown in (b). Numbered labels correspond to those in Table 1. Note that channel #1 does not have depth variation. (c) Extended focus imaging (EFI) microscope image of a fabricated PDMS chip (top) and still frame of sealed PDMS chip during imbibition experiment (bottom).

double-casting to extend the life of the molds or produce chips in alternative polymers. DLW has previously been used in conjunction with soft lithography to produce microfluidic chips, mainly for applications in the life sciences[26,35–37] and microdroplet handling.[38] Our method is tailored for rock-on-a-chip studies of transport phenomena in 2.5D microchannels and networks. The method advances upon previous 2.5D rock-on-a-chip fabrication techniques through greater customization of geometries, finer control of feature sizes and surface properties, and reduced fabrication costs through the reusability of molds. We showcase a multiphase flow experiment in the chips that highlights the influence of capillary action on trapped gas dissolution dynamics in 2D *versus* 2.5D pore confinements, relevant to CO_2 dissolution dynamics in subsurface carbon storage[9,41] and beyond.

Methods

2.5D microfluidic design

A central array of 450-μm-long 2.5D microchannels with varied cross sections and constrictions (down to 1 μm) spans the prongs of an outer U-shaped fluid supply channel (Fig. 1b). The central array is designed to fit within the 750 μm × 500 μm field-of-view of an Olympus MX61A optical microscope using the MPlanFL N 20× objective. The array features converging/diverging channels of rectangular, triangular, and semicircular cross sections that emulate idealized granular pore "throats" in conventional sedimentary rocks (Table 1 and Fig. 1b, channels #1 through #5), and triplicates of straight channels of different cross sections to represent idealized grain boundaries and microfractures in unconventional dual-porosity media such as

Table 1 Description of channel geometries of central array as labelled in Fig. 1. All channels are 450 μm in length

Channel number	Cross section	Width variation	Depth variation	CAD cross-section
1	Rectangle	100 μm wide at ends, tapering along an arc to 2 μm in the middle	50 μm deep throughout	
2	Rectangle	100 μm wide at ends, tapering along an arc to 2 μm in the middle	50 μm deep at ends, tapering along an arc to 1 μm in the middle	
3	Isosceles triangle	100 μm wide base of triangle at ends, tapering along an arc to 2 μm in the middle	50 μm triangle height at ends, tapering along an arc to 1 μm in the middle	
4	Semicircle	100 μm diameter (50 μm depth) at ends, tapering along an arc to 2 μm diameter (1 μm depth) in the middle		
5	Semicircle	100 μm diameter (50 μm depth) at ends, tapering along an arc to 10 μm diameter (5 μm depth) in the middle		
6	Semicircle	2 μm diameter (1 μm depth) throughout		
7	Semicircle	5 μm diameter (2.5 μm depth) throughout		
8	Isosceles triangle	5 μm wide base throughout	2.5 μm triangle height throughout	
9	Semicircle	10 μm diameter (5 μm depth) throughout		

shales, basalts, and other mafic/ultramafic rocks (Table 1 and Fig. 1b, channels #6 through #9). The channel array approach is used for controlled study of pore-confinement effects.[3,4,42,43]

Additional fluid supply channels extend perpendicularly from each side of the U-shaped channel; these channels end in arrow-shaped "punch guides" (Fig. S2a, SI) that indicate locations to place outlets in the PDMS chip later in the fabrication process. All fluid supply channels, including the U-shaped channel, have 50 μm-square cross sections. This design enables study of (1) imbibition/drainage or mixing in the central microchannel array when injecting fluids using the top or bottom outer channels and (2) gas/liquid partitioning by trapping bubbles using the lateral outer channel. The overall span of the U-shaped channel can be redesigned depending on experimental needs (*i.e.*, to fit within a different microscope field-of-view), within the limits of the DLW substrate size.

Importantly, the area within the U-shaped channel can be customized to any geometry that DLW can produce (such as more complex pore-throat networks), as long as there are no overhanging parts that would hinder PDMS demolding. Thus, the presented method presents a major advancement opportunity for rock-on-a-chip microfluidics, which typically feature 2D periodic shapes such as disks to represent grains[17,44,45] or more irregular grain size distribution patterns inspired by tomograms or thin sections.[18,46] In such cases, all features are the same height and cross section and are more akin to Hele-Shaw cells with obstacles.

Microfluidic chip fabrication with precision nanoscale features

CAD software (Autodesk Fusion) was used to create the positive geometry shown in SI Fig. S2a and S2c (see also CAD file included in SI). The design was converted to laser writing files with the DeScribe software (Nanoscribe GmbH). To reduce printing time, higher-resolution print settings were used for the central channels while lower-resolution settings were used for all other parts of the geometry. The selected settings resulted in controlled nanoscale surface steps within the microchannels and can be used as a technique to generate controlled surface features/roughness on the scale of 100s of nanometers (Fig. S3 in SI).

The microfluidic geometry was printed with the commercial IP-S photoresist (Nanoscribe GmbH) and the 25× objective using a Nanoscribe Photonic Professional GT in the dip-in laser lithography (DiLL) configuration on a 25 mm × 25 mm × 0.7 mm (thickness) glass substrate coated with indium-tin oxide (ITO). Printing time lasted approximately 40 minutes. Fig. S2b and S2d in the SI show the resulting print. Fig. 2 details the soft lithography steps implemented to make microfluidic chips from the DLW master pattern. PDMS (Sylgard 184, Dow Corning) in a 15 : 1 base-monomer-to-crosslinker ratio was cast on top of the DLW mold inside a 3D-printed mold frame, resulting in a PDMS cast with the negative (inverse) geometry of the DLW print (Fig. 1c, 2b and 3; see Fig. S4 in SI for additional SEM characterization). This PDMS cast can be directly used as a microfluidic chip after creating inlets/outlets and sealing with O_2 plasma bonding (see Fig. 2 and Fig. S6a, SI).

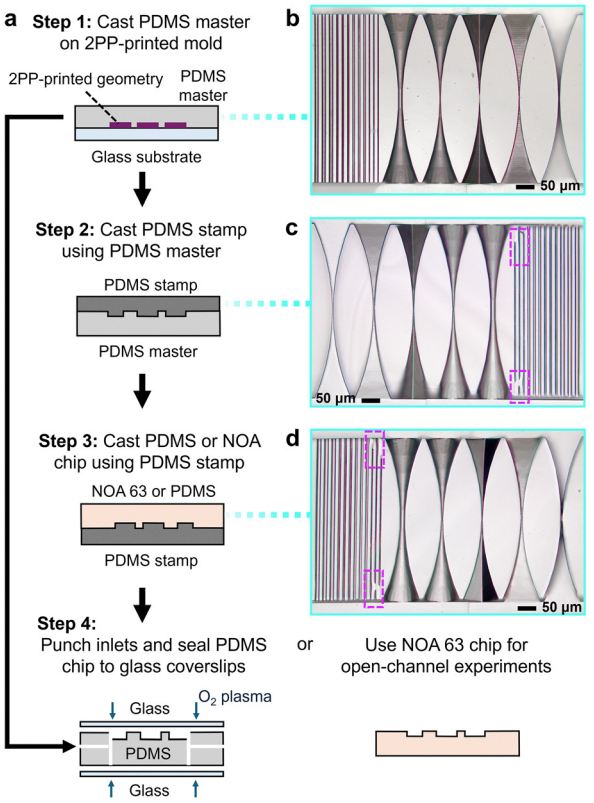

Fig. 2 (a) Schematic diagram of fabrication workflow. PDMS casted on DLW-printed molds (Step 1) can be turned directly into a microfluidic chip (Step 4) or used as a master for double-casting (Steps 2–4). Microscope images using extended focused imaging (EFI) of the central channels associated with each step: (b) PDMS casted on a DLW-printed mold; (c) a PDMS stamp casted on a PDMS master; (d) an NOA 63 chip casted on a PDMS stamp. Pattern details were well preserved during soft lithography, except for areas highlighted by dotted rectangles in (c) and (d) where delicate features did not successfully replicate when casting the PDMS stamp. These defects were then propagated into the NOA 63 chip.

Alternatively, the PDMS cast can itself be used as a master pattern and replicated through double casting to create a microfluidic chip. This technique can be useful to prolong the life of the original DLW print, or to create microfluidic chips of a different polymer material (Fig. 2; see SI Section 2.2 for a summary of double casting procedure and success). To demonstrate fabrication of chips using a different polymer, Norland Optical Adhesive (NOA) 63 (Norland Products), a transparent UV-curable adhesive, was cast on the PDMS stamp and cured with a 365 nm lightsource for 30 minutes (Fig. 3d). Additional details on 2.5D microfluidic design and chip fabrication methodology can be found in SI, Section 2.

Surface roughness characterization

Surface roughness directly impacts wettability,[47] capillary trapping,[48] and multiphase flow patterns.[17] Fig. 3 highlights the control over surface texture enabled through combining DLW and soft lithography. This texture is composed of regular ridges that are distinct from the smooth texture of PDMS that was in contact with the glass substrate when cast, as can be

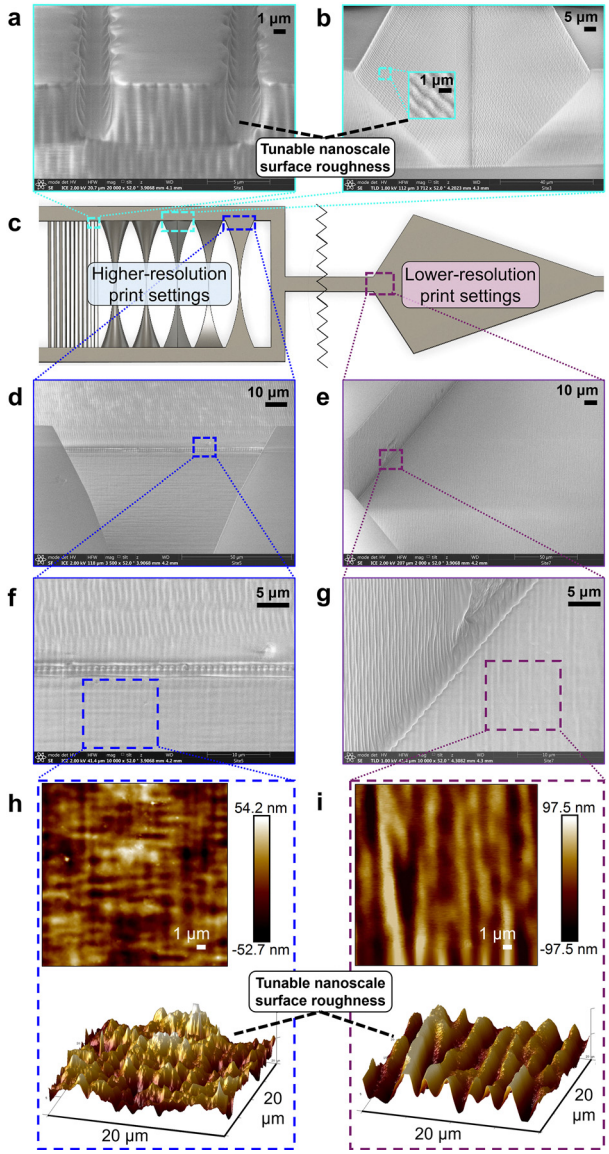

Fig. 3 Surface feature characterization of an open PDMS chip casted on the DLW-printed mold. Scanning electron microscopy (SEM) images (FIB-X Services, Plano, TX) of regular, submicron ridges along the walls of (a) channels #6 and (b) channel #3. (c) CAD schematic highlighting characterized areas. Channels in the U-shape section (left) were printed with higher-resolution settings while all other sections were printed with lower-resolution settings (right), resulting in differences in the submicron ridges generated by the DLW print. These patterns are transferred to the PDMS cast as seen in the SEM in (d)–(g). Atomic force microscopy (AFM) characterization of (h) NOA casted directly on channel #1 of the PDMS cast and (i) an arrow-shaped punch guide of the PDMS cast. The positive NOA cast was used for the AFM measurement in (h) due to difficulties measuring inside the PDMS channels, but still corroborates the surface features seen in (f).

seen by textural differences within and between the channels shown in Fig. 3a. The ridges, while present in all channels, are more prominent on channel walls and sloped areas as compared to flat sections. Fig. 3d–i compares the textures of flat channels in a PDMS chip resulting from different sections of the DLW mold with higher and lower print resolutions. The height of the surface texture of the lower resolution section is ~200 nm, roughly twice that of the higher resolution section. The width of a ridge is approximately 1 μm, as shown by the AFM measurements in Fig. 3h and i. The higher-resolution section shows a prominent crosshatch pattern, while the lower-resolution section shows monodirectional ridges with a slightly larger amplitude and wave period. Additional SEM images highlighting channel surface texture are shown in SI Fig. S4.

Replicability

We find that a single DLW mold can be reused multiple times (5× tested herein) without degrading the mold. 15 : 1 PDMS casted directly on the DLW prints consistently resulted in successful transfer of the microfluidic geometry when examined under a cleanroom-grade Olympus MX61A optical microscope (Fig. 2b and Fig. S5c, d, SI). Note that the double casting technique was slightly more prone to imperfections in replicating the most delicate geometries, as was the case with the 1-μm tall straight channels in Fig. 2c. These defects are then replicated in the NOA 63 cast seen in Fig. 2d. Tall, thin geometries (such as the pinch point of channel #1) are particularly susceptible to defective replication during double casting. Treating the PDMS master with hexamethyldisilazane (HMDS) and the inclusion of multiple instances of delicate geometries in the design helps to increase the odds of successful replication of these geometries.

Experimental verification

Lab-on-a-chip demonstration

The functionality and satisfactory bonding of multiple PDMS-glass microfluidic chips was demonstrated through water-air imbibition and drainage experiments (Fig. 4). Tubing (1.32 mm outer diameter, Scientific Commodities) slightly larger than the inlet/outlet holes was inserted into the lateral inlet (Fig. S6a, SI); the flexibility of PDMS generated a seal around the tubing. A syringe connected to the other end of the tubing was used to manually introduce deionized (DI) water into the lateral outer channel of an initially dry chip (Fig. S6b, SI). Once water was in the lateral outer channel, the chip and connected syringe were left undisturbed, initiating spontaneous imbibition at ambient temperature and pressure in the U-shaped supply channel and 2.5D microchannel array (Fig. 4). Video of fluids in the central microchannel array was captured using an Olympus MX61A optical microscope in brightfield mode (SI Video A). Fig. 4c–e shows images from the imbibition process, whereby air bubbles were successfully trapped in the array by fluid imbibing in parallel through the prongs of the U-shaped supply channel. Small pockets of condensation (<1 μm, with some growing up to 25 μm in diameter) nucleated rapidly within the trapped bubbles, often on points of imperfection assumed to be from particulates incorporated into the casting process (see Fig. 4e and cyan boxes in Fig. 4c). These droplets indicate a net increase in confined bubble pressure that exceeded the ambient vapor

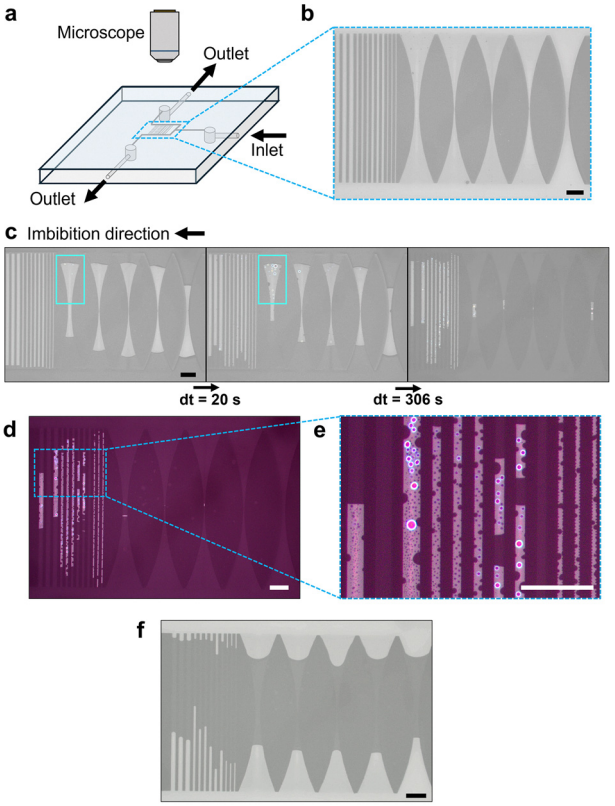

Fig. 4 (a) Schematic of experimental setup for imbibition and drainage experiments in a PDMS-glass chip. Brightfield microscope images of the microfluidic chip (b) before imbibition, (c) during imbibition, and (d and e) at steady state ~30 min after commencing imbibition show air bubbles trapped by liquid in the central channels. The cyan rectangles in (c) point out water condensation inside the air bubbles. (f) Brightfield microscope image of a drainage experiment, in which liquid was trapped inside the central channels. All scale bars are 50 μm.

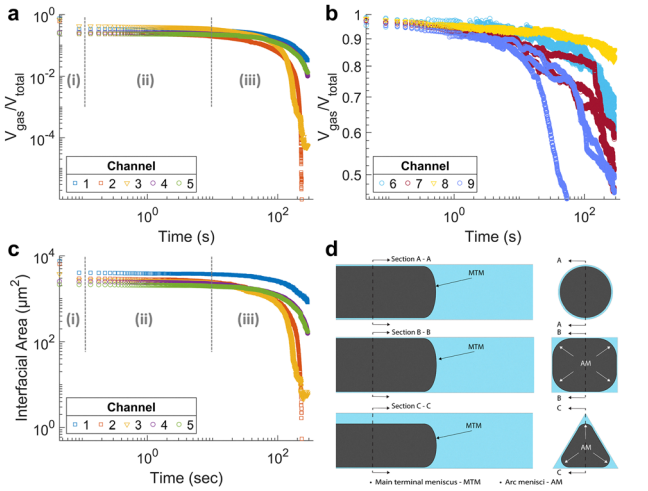

Fig. 5 Normalized trapped gas volume over time for (a) channels #1–#5 and (b) channels #6–#9; note that channels #6–#9 have triplicates of each. (c) Gas–liquid interfacial area (IA) of trapped gas bubble over time for channels #1–#5. (d) Schematic of menisci during drainage in circular, rectangular, and triangular channels showing the effect of corners, adapted from Li and Yao.[51] For channels #1–#5, panels (a) and (c) reveals three dissolution regimes: (i) at initial times (<0.1 s) there is an initial capillary jump regime where fluids rapidly fill the channels from both sides; (ii) next, at early times (~<10 s) there is a temporary quasi-equilibrium compression period where bubble size and IA change minimally according to a power-law trend (*i.e.*, linear in log–log space); (iii) at later times (~>10 s) and for the remainder of the experiment (~5 min), bubble dissolution proceeds with complex non-linear dynamics (*i.e.*, curved in log–log space), indicating a non-power-law function or piece-wise varying rates of change. Panel (b) shows that bubble dissolution in the narrow straight channels also follow a temporary quasi-equilibrium period until a certain time followed by a more piece-wise or fragmented regime. These narrow channels are more subject to capillary pinning due to the larger size of the precision surface roughness relative to the overall channel size.

pressure of water. Following imbibition, a coarse drainage experiment was performed by using a syringe to manually push air into the lateral outer channel of the same chip (SI Video B); Fig. 4f shows trapped liquid plugs in the central channels. No leakage at the tubing-chip connection or the PDMS-glass interfaces was observed.

2.5D confinement influences on bubble dissolution dynamics

The imbibition experiment demonstrates that 2.5D cross-sectional geometry and channel convergence strongly influence bubble dissolution rate, particularly when comparing channels with higher-curvature menisci due to corners (*i.e.*, triangular cross section, channel #3). Fig. 5 displays the change in the temporal gas–water interfacial area (IA) and normalized volume of trapped bubbles within Table 1 channels, as quantified with image analysis described in Section 4 of the SI. Channel #1 is a 2D rectangular channel converging in one direction (x–y plane), which represents a conventional microfluidic geometry baseline. Fig. 5 caption summarizes the observed dissolution regimes, with all channels experiencing non-linear bubble dissolution dynamics after initial compression. We expect the balance of capillary pressure (P_c) and viscous pressure losses (ΔP) to drive the rate of bubble dissolution. The Young–Laplace equation describes capillary pressure across an interface by[49]

$$P_c = \gamma\left(\frac{1}{r_1}+\frac{1}{r_2}\right) \quad (1)$$

where γ is the gas–liquid surface tension and r_1 and r_2 are the principal radii of curvature of the interface. Viscous pressure losses for pressure-driven flow are defined by the Hagen–Poiseuille equation:[3,50]

$$\Delta P = \frac{\mu}{k}u(t)l(t) \quad (2)$$

where μ is viscosity, k is a geometric term related to the channel's cross-sectional shape, and the average velocity u and length of imbibed fluid l are functions of time t. P_c and ΔP create a pressure differential that drives gas molecules from the bubble into the surrounding liquid per Henry's Law:

$$P_b = \frac{c_a}{k_H} \quad (3)$$

where P_b is the equilibrium pressure in the bubble, c_a is the concentration of air dissolved in the imbibing liquid, and k_H is the Henry solubility constant. The mass transfer rate $\frac{dM}{dt}$ across

the gas–liquid interfaces is given by

$$\frac{dM}{dt} = -k_L A(c_{eq} - c_a) \quad (4)$$

where k_L is the gas–liquid mass transfer coefficient, A is the gas–liquid interfacial area (IA), and c_{eq} is the equilibrium concentration of air in the imbibing liquid. Unlike bubbles floating in bulk, as a channel-trapped bubble shrinks, its IA will not necessarily decrease in proportion to its volume – this relationship is a function of the confinement geometry.

ΔP increases in all channels with time and is greatest in the straight narrow channels (#6 to #9). In the 2.5D converging channels (#2 to #5), a rapid decrease in channel cross-sectional area corresponds to a rapid increase in P_c, but a decrease in IA and mass transfer. In accordance, the trapped bubbles in these channels steadily dissolved on the order of minutes, with the fastest dissolution in channels #2 (rectangular) and #3 (triangular). These channels have more corners and higher capillary curvature than their semi-circular counterparts (#4 and #5).[52] Bubble dissolution in channel #1 is slower than all of the 2.5D converging channels. As a 2D converging channel, channel #1 has the lowest overall capillary pressure and the lowest viscous losses. In contrast, bubbles in the narrow straight channels (channels #6 to #9) reached a steady state (with bubbles still remaining) approximately 30 minutes after the start of imbibition. P_c is high but roughly constant in these conduits and bubble dissolution is tempered by a much higher ΔP and consistently low IA. Within early times ($\sim <10$ seconds), the relative volume of gas in channels #6 decreased the slowest, followed by channels #8 (triangular) and then the semi-circular channels #7 and #9. This order is in accordance with decreasing ratio of wetted perimeter to cross-sectional area and, therefore, decreasing ΔP. At late times, the spread of bubble dissolution data among the narrow channel triplicates is greatest in channel sets #7 and #9. These semi-circular channels are the largest of the narrow channels, so a moving meniscus can more easily overcome pinning due to surface roughness and corners.[53]

Overall, the example microfluidic experiment reveals *capillary-driven* and *viscous-tempered* bubble dissolution regimes: In channel geometries representing converging sandstone pore throats (channels #1–#5), bubble dissolution proceeds in a positive feedback loop where capillary pressure increases as the trapped bubble shrinks, further accelerating dissolution with time. However, for near-sub-micron conduits more accurately representing narrow grain boundaries in tighter unconventional rocks (channels #6–#9), higher viscous pressure losses dominate and temper bubble dissolution. Both regimes were sensitive to differences in cross-sectional geometry. Future works will employ analytical frameworks coupling liquid imbibition in converging channels with trapped gas pressure and mass transport (similar to Kelly *et al.*[3]) to extract values for scalable parameters (*e.g.*, gas partitioning and diffusion) from the experimental results. Experiments emerging from these methods can also be used as benchmarks for pore-scale computational fluid dynamics simulations; in particular, the stepped CAD geometry replicated with DLW is directly transferable to the voxelated geometries used in Lattice Boltzmann method simulations.[54–56]

Further discussion of recommended pore-scale transport phenomena studies using the featured microfluidic chip and workflow are detailed in the SI, Section 5.

Author contributions

Both K. Y. and S. K. performed conceptualization, microfluidic chip and experimental design, data analysis, and writing of the manuscript. K. Y. performed CAD design, chip fabrication methodology, experimental verification, and quantitative image analysis. S. K. also provided supervision and project management.

Conflicts of interest

There are no conflicts to declare.

Data availability

The data supporting this article have been included as part of the supplementary information (SI). Supplementary information: further fabrication and experiment details, STL file of the featured geometry, and Videos A and B of the imbibition and drainage experiments, respectively. See DOI: https://doi.org/10.1039/d5sm01004g.

Acknowledgements

The design and generation of 2.5D microfluidic devices with precision nanoscale features by K. Y. & S. K. was supported by the U.S. Department of Energy, Office of Science, Office of Basic Energy Sciences, Geosciences program under Award Number DE-SC0025348. Graduate student support was also provided in part by the donors of the American Chemical Society Petroleum Research Fund (ACS PRF) under Grant #66777-DNI9. This work was performed in part at the Nanofabrication Facility at the Advanced Science Research Center at The Graduate Center of the City University of New York. The authors also acknowledge the use of facilities and instrumentation supported by NSF through the Columbia University, Columbia Nano Initiative, and the Materials Research Science and Engineering Center DMR-2011738. We are grateful to labmates Rosalie Krasnoff for acquisition of channel SEM images and Tianxiao Shen for AFM characterization. We also thank Richard San Martin and FIB-X Services (Plano, TX) for field-emission SEM acquisition.

References

1 Y. Zhuang, G. Zhu, Y. Jin, M. Qu, Q. Lin and L. Zeng, *J. Hydrol.*, 2024, **640**, 131675.
2 J. Poonoosamy, C. Soulaine, A. Burmeister, G. Deissmann, D. Bosbach and S. Roman, *Lab Chip*, 2020, **20**, 2562–2571.

3 S. Kelly, M. T. Balhoff and C. Torres-Verdín, *Langmuir*, 2015, **31**, 2167–2179.
4 B. Bao, S. H. Zandavi, H. Li, J. Zhong, A. Jatukaran, F. Mostowfi and D. Sinton, *Phys. Chem. Chem. Phys.*, 2017, **19**, 8223–8229.
5 M. A. Chen, S. H. Lee and P. K. Kang, *Proc. Natl. Acad. Sci. U. S. A.*, 2024, **121**, e2407145121.
6 H. Zhang, Z. Sun, N. Zhang and B. Zhao, *Water Resour. Res.*, 2024, **60**, e2023WR035670.
7 M. Maleki, H. Mehrjoo, Y. Kazemzadeh, F. Mohmmadinia and A. Ranjbar, *Environ. Earth Sci.*, 2025, **84**, 60.
8 K. Komnitsas, D. Zaharaki, G. Bartzas and G. Alevizos, *Minerals*, 2017, **7**(10), DOI: 10.3390/min7100200.
9 T. Shen, Q. R. S. Miller, N. Lahiri, O. Terry, A. T. Owen, Z. Kou, H. T. Schaef and S. A. Kelly, *Environ. Sci. Technol.*, 2025, **59**(38), 20345–20356.
10 H. Nisbet, R. Li, P. Purswani, M. Chen, W. Yang, C. Neil, Q. Kang, K. Mohanty, P. K. Kang and H. Viswanathan, *Lab Chip*, 2025, **25**, 4024–4037.
11 M. D. Aliyu and H.-P. Chen, *Energy*, 2018, **165**, 931–948.
12 Y. Pan, J. Yang, Y. Jia and Z. Xu, *Environ. Earth Sci.*, 2015, **75**, 75.
13 H. Yang, X. Min, S. Xu, J. Bender and Y. Wang, *ACS Sustainable Chem. Eng.*, 2020, **8**, 2531–2539.
14 G. Akay, M. A. Bokhari, V. J. Byron and M. Dogru, *Chem. Eng.*, 2005, 171–197.
15 G. Pontrelli and F. de Monte, *Int. J. Heat Mass Transfer*, 2007, **50**, 3658–3669.
16 M. Fourmentin, P. Faure, S. Rodts, U. Peter, D. Lesueur, D. Daviller and P. Coussot, *Cem. Concr. Res.*, 2017, **95**, 56–64.
17 A. Mehmani, S. Kelly, C. Torres-Verdín and M. Balhoff, *Fuel*, 2019, **251**, 147–161.
18 S. A. Kelly, C. Torres-Verdín and M. T. Balhoff, *Lab Chip*, 2016, **16**, 2829–2839.
19 K. Xu, T. Liang, P. Zhu, P. Qi, J. Lu, C. Huh and M. Balhoff, *Lab Chip*, 2017, **17**, 640–646.
20 D. J. Harrison, K. Fluri, K. Seiler, Z. Fan, C. S. Effenhauser and A. Manz, *Science*, 1993, **261**, 895–897.
21 S. C. Jacobson, R. Hergenroeder, L. B. Koutny and J. M. Ramsey, *Anal. Chem.*, 1994, **66**, 2369–2373.
22 A. Massimiani, F. Panini, S. L. Marasso, M. Cocuzza, M. Quaglio, C. F. Pirri, F. Verga and D. Viberti, *Water*, 2023, **15**(6), DOI: 10.3390/w15061222.
23 C. M. Leung, P. de Haan, K. Ronaldson-Bouchard, G.-A. Kim, J. Ko, H. S. Rho, Z. Chen, P. Habibovic, N. L. Jeon, S. Takayama, M. L. Shuler, G. Vunjak-Novakovic, O. Frey, E. Verpoorte and Y.-C. Toh, *Nat. Rev. Methods Primers*, 2022, **2**, 33.
24 Y. Huang, T. Liu, Q. Huang and Y. Wang, *ACS Sens.*, 2024, **9**, 3466–3488.
25 C. Duan, W. Wang and Q. Xie, *Biomicrofluidics*, 2013, **7**, 026501.
26 O. M. Young, X. Xu, S. Sarker and R. D. Sochol, *Lab Chip*, 2024, **24**, 2371–2396.
27 C. A. Conn, K. Ma, G. J. Hirasaki and S. L. Biswal, *Lab Chip*, 2014, **14**, 3968–3977.
28 B. Callow, I. Falcon-Suarez, H. Marin-Moreno, J. M. Bull and S. Ahmed, *Geophys. J. Int.*, 2020, **223**, 1210–1229.
29 H. Sun, S. Vega and G. Tao, *J. Pet. Sci. Eng.*, 2017, **156**, 419–429.
30 W. Lei, X. Lu, W. Gong and M. Wang, *Proc. Natl. Acad. Sci. U. S. A.*, 2023, **120**, e2310584120.
31 S. N. Khonina, N. L. Kazanskiy and M. A. Butt, *Micromachines*, 2024, **15**, 1321.
32 A. Naillon, H. Massadi, R. Courson, J. Bekhit, L. Seveno, P. F. Calmon, M. Prat and P. Joseph, *Microfluid. Nanofluid.*, 2017, **21**, 131.
33 Nanoscribe, Setting standards for 3D nano- and microfabrication for 15 years, https://www.nanoscribe.com/en/news-insights/news/nanoscribe-15-year-anniversary/, (accessed August 15, 2025).
34 S. Kawata, H.-B. Sun, T. Tanaka and K. Takada, *Nature*, 2001, **412**, 697–698.
35 Z. Faraji Rad, R. E. Nordon, C. J. Anthony, L. Bilston, P. D. Prewett, J.-Y. Arns, C. H. Arns, L. Zhang and G. J. Davies, *Microsyst. Nanoeng.*, 2017, **3**, 17034.
36 R. Šakalys, K. W. Kho and T. E. Keyes, *Sens. Actuators, B*, 2021, **340**, 129970.
37 R. Soffe, S. Baratchi, M. Nasabi, S.-Y. Tang, A. Boes, P. McIntyre, A. Mitchell and K. Khoshmanesh, *Sens. Actuators, B*, 2017, **251**, 963–975.
38 H. Zhang, C. Huang, Y. Li, R. Gupte, R. Samuel, J. Dai, A. Guzman, R. Sabnis, P. de Figueiredo and A. Han, *Sci. Adv.*, 2022, **8**(27), eabc9108.
39 S. Kelly, H. El-Sobky, C. Torres-Verdín and M. T. Balhoff, *Adv. Water Resour.*, 2016, **95**, 302–316.
40 M. J. Blunt, B. Bijeljic, H. Dong, O. Gharbi, S. Iglauer, P. Mostaghimi, A. Paluszny and C. Pentland, *Adv. Water Resour.*, 2013, **51**, 197–216.
41 S. Bakhshian, *Int. J. Greenhouse Gas Control*, 2021, **112**, 103520.
42 K. K. Rangharajan and S. Prakash, *Analyst*, 2025, **150**, 2837–2844.
43 K. Morikawa, Y. Kazoe, K. Mawatari, T. Tsukahara and T. Kitamori, *Anal. Chem.*, 2015, **87**, 1475–1479.
44 C. A. Conn, K. Ma, G. J. Hirasaki and S. L. Biswal, *Lab Chip*, 2014, **14**, 3968–3977.
45 W. Xu, J. T. Ok, F. Xiao, K. B. Neeves and X. Yin, *Phys. Fluids*, 2014, **26**, 093102.
46 A. Kharrat, B. Brandstätter, M. Borji, R. Ritter, P. Arnold, G. Fritz-Popovski, O. Paris and H. Ott, *J. Colloid Interface Sci.*, 2022, **608**, 1064–1073.
47 J. Botto, S. J. Fuchs, B. W. Fouke, A. F. Clarens, J. T. Freiburg, P. M. Berger and C. J. Werth, *Energy Fuels*, 2017, **31**, 5275–5285.
48 H. Geistlinger, I. Ataei-Dadavi and H.-J. Vogel, *Transp. Porous Media*, 2016, **112**, 207–227.
49 P. Abgrall, *Nanofluidics*, Artech House, Boston, 2009.
50 R. B. Bird, W. E. Stewart and E. N. Lightfoot, *Transport Phenomena*, John Wiley & Sons, 2007.
51 G. Li and J. Yao, *Eng*, 2023, **4**, 2896–2925.
52 N. Kubochkin and T. Gambaryan-Roisman, *Curr. Opin. Colloid Interface Sci.*, 2022, **59**, 101575.

53 B. M. Mognetti and J. M. Yeomans, *Phys. Rev. E: Stat., Nonlinear, Soft Matter Phys.*, 2009, **80**, 056309.
54 M. C. Sukop and D. T. Thorne, *Lattice Boltzmann Modeling*, Springer, 2006.
55 J. E. McClure, Z. Li, M. Berrill and T. Ramstad, *Comput. Geosci.*, 2021, **25**, 871–895.
56 P. Pradhan, P. Gentine and S. Kelly, *J. Adv. Model. Earth Syst.*, 2026, **18**, e2025MS005313.